Multiscale influence of trace Tb addition on the magnetostriction and ductility of ⟨100⟩ oriented directionally solidified Fe-Ga crystals

Yuye Wu,[1,*] Yijun Chen,[1] Chongzheng Meng,[1] Hui Wang,[1] Xiaoqin Ke,[2] Jingmin Wang,[1] Jinghua Liu,[1] Tianli Zhang,[1] Ronghai Yu,[1] J. M. D. Coey,[1,3] Chengbao Jiang,[1,†] and Huibin Xu[1]

[1]*Key Laboratory of Aerospace Materials and Performance (Ministry of Education), School of Materials Science and Engineering, Beihang University, Beijing 100191, People's Republic of China*

[2]*Frontier Institute of Science and Technology, State Key Laboratory for Mechanical Behavior of Materials, Xi'an Jiaotong University, Xi'an, People's Republic of China*

[3]*School of Physics and CRANN, Trinity College, Dublin 2, Ireland*

(Received 24 April 2018; revised manuscript received 16 August 2018; published 15 March 2019)

New-generation magnetostrictive applications in micromanipulation instruments, torque sensing, and transducers require materials that offer a combination of large magnetostriction and good structural properties. $Fe_{100-x}Ga_x$-based ($x = 17$–19) alloys are potential candidates. In this work, the solidification behavior of Tb-doped FeGa alloys is investigated by theoretical simulation and experimental observation; directional solidification parameters are optimized to obtain the largest solid solubility of Tb while keeping the ⟨100⟩ preferred orientation. The multiscale evolution of the structure with Tb additions that enhances both magnetostriction and tensile properties is systematically studied in alloys prepared under optimal directional solidification conditions. Magnetostriction of 387 ppm is accompanied by a remarkable tensile fracture strain of 12.5% in 0.05 at.% Tb-doped $Fe_{81}Ga_{19}$. The values represent an improvement of ∼29% in magnetostriction and a sixfold enhancement in tensile fracture strain compared with undoped binary $Fe_{81}Ga_{19}$. The increase in magnetostriction is attributed to the higher density of tetragonally modified $D0_3$ nanoinclusions induced by traces of Tb. The enhancement in ductility is explained by the dislocation concentration around the submicron-scale Tb-rich precipitates which can effectively hinder their motion. The FeGa alloys doped with traces of Tb can be easily processed to thin sheets or wires and are likely to be extensively applied because they contain only traces of rare earths.

DOI: 10.1103/PhysRevMaterials.3.033401

I. INTRODUCTION

Magnetostrictive materials have attracted considerable attention due to their increasingly important role in micromanipulations, torque sensing, liquidometers, and ultrasonic transducers [1–6]. Their performance has been gradually optimized in recent decades [1,2,7,8]. For a long time, a large magnetostriction and excellent ductility were contradictory requirements. The Fe/Ni-based alloys possess superb ductility, allowing them to be processed to thin sheets and wires [9–13], but their magnetostriction does not exceed 100 ppm, which precludes applications where a large value is required. The (TbDy)Fe_2 alloys have been found to offer giant magnetostriction of over 1000 ppm with minimum cubic anisotropy, but at a high cost for the heavy rare earths [8,14,15]. Furthermore, the brittleness of the Laves phase alloys mean that they fracture in tension and cannot be processed into other shapes. They are used in the form of oriented rods prepared by directional solidification [3,16]. A severe problem for magnetostrictive materials during normal operation is eddy-current loss in high-frequency alternating magnetic fields, which is proportional to the thickness of the magnetostrictive laminations. Sheets or wires have advantages in many applications. For example, high-power ultrasonic transducers based on magnetostrictive sheets can play a key role in nondestructive flaw detection, thanks to the low eddy-current loss. Another example is the liquid level sensor, which requires wires with large magnetostriction, so a combination of large magnetostriction and good ductility is essential. Therefore, combining large magnetostriction with significantly better mechanical properties and low cost is a significant step towards realizing devices that integrate structural integrity and magnetostrictive functionality [1,4]. Figure 1 illustrates the payoff between magnetostriction and mechanical properties of the materials we discuss, and it situates the Fe-Ga alloys doped with traces of Tb that we have prepared in the present work [7,11,17–26].

The RE-free FeGa magnetostrictive alloys, discovered in 2000, offer a combination of large magnetostriction (approximately 300 ppm for $Fe_{81}Ga_{19}$ single crystals [27]) and moderate fracture strain (∼0.3% for polycrystals and ∼2% for single crystals [22,28,29]). Moreover, the saturation field of all FeGa rods is rather low (<300 Oe) [23,30]. These advantages make the alloys interesting for new-generation magnetostrictive applications. Even so, their ductility is insufficient for some processes such as rolling, forging, and wire drawing, and a still larger magnetostriction would be welcome. Boron or carbide (NdC, TaC) dopants improve the magnetostriction and mechanical properties simultaneously, but the gains are not large [21,24,31–36]. Alloying *p* or *d* elements such as

*Corresponding author: wuyuye@buaa.edu.cn
†jiangcb@buaa.edu.cn

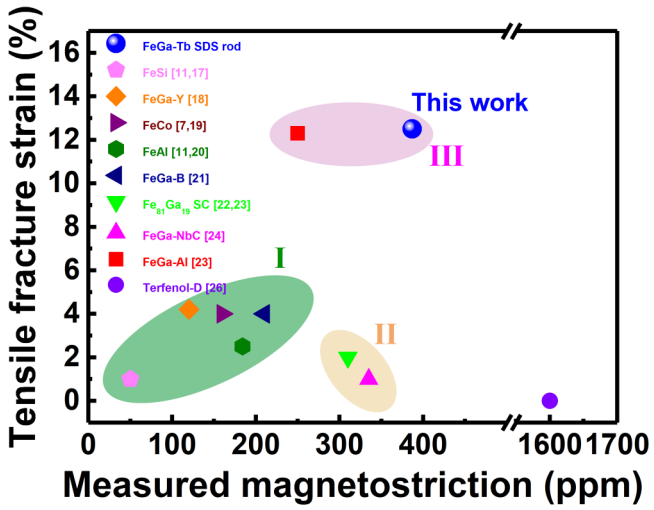

FIG. 1. Summary of measured magnetostriction and tensile fracture strain for common Fe-based magnetostrictive materials and Terfenol-D. SC: single crystal.

Mn, Mo, Co, Ni, Al, and Zn can significantly enhance the mechanical properties, but generally do nothing to improve the magnetostrictive performance [34,35,37–39]. Recent research has concentrated on the surprising effects of trace rare-earth (RE) doping [40,41], and it has been discovered that the magnetostriction can be enhanced to more than 600 ppm in melt-spun FeGa ribbons containing Pr, Tb, Dy, or some other rare-earth elements [41–43]. This enhancement has been attributed to the tetragonal distortion of the matrix induced by the solid solubility of traces of RE atoms [41–45]. Besides the significant improvement in magnetostriction, RE simultaneously benefits the mechanical properties. In as-cast $Fe_{83}Ga_{17}$ alloy, a 0.2 at.% addition of Tb or Y can induce a transition from brittle to ductile fracture, with a tensile strain of 4%, nearly ten times larger than binary polycrystalline material [18,29]. The simultaneous improvement in magnetostriction and ductility opens some new possibilities for applications. Oriented rods are required for FeGa alloy-based actuators because the magnetostriction of FeGa is anisotropic and largest along the ⟨100⟩ directions [3,23,46,47]. Directional solidification (DS) is the key technology for preparing rods with the necessary orientation, so RE doping has to be incorporated. This is the focus of our work: we first investigate the evolution of microstructure and magnetostriction under different withdrawal rates in order to determine the optimal conditions by simulation and experiment. Then we prepare $Fe_{83}Ga_{17}$ and $Fe_{81}Ga_{19}$ alloys with different small Tb concentrations under optimal conditions and study the variation of magnetostriction and tensile properties. Finally, we explain the mechanism whereby traces of Tb simultaneously enhance magnetostriction and ductility, acting on quite different length scales, and discuss the implications for magnetostrictive applications.

II. EXPERIMENTS

Master alloys with nominal atomic composition $(Fe_{83}Ga_{17})_{100-x}Tb_x$ $(x = 0, 0.05, 0.1, 0.2, 0.5)$ and $(Fe_{81}Ga_{19})_{100-x}Tb_x$ $(x = 0, 0.05, 0.1)$ were prepared by vacuum arc melting under Ar atmosphere. Mixtures of constituent elements with purity greater than 99.99% were melted with a 2% excess of Ga. Ingots were remelted four times to ensure homogeneity and then cast in a chilled copper mold to obtain master rods with a diameter of 7 mm and length of about 150 mm. Directional solidification at growth rates of 25, 3000, and 6000 mm/h was predicted using PROCAST software, which allows the modeling of thermal heat transfer including radiation fluid flow with the thermal solution using the finite-element method (FEM). The simulation parameters of Fe-Ga alloys are selected from the report by Elliott *et al.* [48].

Directional solidification was used to prepare Tb-doped $(Fe_{83}Ga_{17})_{99.9}Tb_{0.1}$ rods at withdrawal rates of 25, 500, 1500, 3000, or 6000 mm/h. Liquid metal with chemical composition $Ga_{68.5}In_{21.5}Sn_{10}$ fills the water-cooled cylinder, where it has no influence of the chemical compositions of the master rods but can create a large temperature gradient near the solid-liquid interface because its thermal conductivity coefficient is as large as $\sim 16.5\,W/m\,K^{-1}$. A series of $(Fe_{83}Ga_{17})_{100-x}Tb_x$ $(x = 0, 0.05, 0.1, 0.2, 0.5)$ and $(Fe_{81}Ga_{19})_{100-x}Tb_x$ $(x = 0, 0.05, 0.1)$ as-cast rods were directionally solidified with a FeGa ⟨100⟩ single-crystal seed at the bottom, using optimal parameters determined by theoretical simulation and previous experiments. The cross-section and longitudinal section surfaces of the rods were ground, polished, and etched with a dilute acid solution (7 ml HCl, 3 ml H_2O_2, and 20 ml H_2O) to reveal the microstructure, which was observed by optical microscopy and JEOL JXA-8100 Electron Probe Microanalysis (EPMA). The average size of the precipitates was analyzed using NANOMEASURE software, and their volume fraction was analyzed by image-recognition technology applied to the EPMA images. The chemical phase compositions were determined with an energy dispersive spectrometer (EDS) in the EPMA. The crystal structure and orientation were identified with a D/max 2500 x-ray diffractometer (XRD) using Cu-K_α radiation ($\lambda = 154.18$ pm) at a scanning speed of 6°/min. The microstructures of the alloys were examined in more detail by JEOL JEM-2100F transmission electron microscopy (TEM). The TEM specimens were prepared from $\sim 100\,\mu$m slices of the rod that were mechanically ground to about 50 μm thick, and thinned by ion milling. Magnetostriction was measured by the standard strain gauge method along the growth direction. Two-dimensional phase-field simulation is performed to explain the mechanism of enhanced magnetostriction in the Tb-doped alloys, considering both magnetization field and composition field. The lattice parameters of the modified-$D0_3$ nanoinclusions are determined from first-principles calculations to be $a = 0.2861$ nm and $c = 0.2867$ nm [42], and Tb solid solution effect on the lattice parameters of modified-$D0_3$ nanoinclusions is ignored because the solubility of Tb is very low. Detailed information on the phase-field simulation method is given in Ref. [42]. Specimens for tensile tests with dimensions 10 mm (length) × 4 mm (width) × 1 mm (thickness) were cut by the electric-spark method along the directional solidification direction. Room-temperature tensile tests were carried out on a computer-controlled Instron-8801 testing machine at a constant stain rate of $1 \times 10^{-4}\,s^{-1}$ and the fracture surfaces were examined using scanning electron microscopy (SEM). One rod with

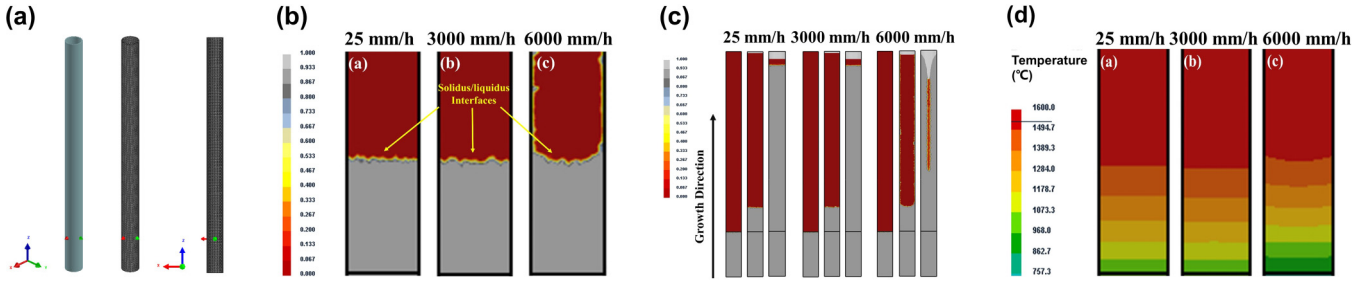

FIG. 2. (a) Finite-element mesh of the rod. The (b) simulated solid-liquid interface morphology, (c) growth process, and (d) temperature contour at the withdraw rates of 25, 3000, and 6000 mm/h.

chemical composition $(Fe_{81}Ga_{19})_{99.95}Tb_{0.05}$ was forged at 1270 K to reduce the thickness to 15 mm. After hot soaking at 1270 K for 1 h, the forged samples were then hot rolled at 1270 K, giving a 70% reduction to a thickness of ~1.7–2 mm. Subsequently, a warm rolling at 720 K was performed to produce a sheet with a thickness of 0.6 mm. After an intermediate annealing at 770 K to release the stress, the sheets were rolled to be thinner than 0.1 mm at room temperature.

III. RESULTS AND DISCUSSION

A. Evolution of directional solidification behavior

In 2008, Lograsso *et al.* investigated the Ga dependence of the magnetostriction in $Fe_{100-x}Ga_x$ ($x = 0$–35) single crystals, observing two magnetostriction peaks appearing in the composition ranges of $x = 17$–19 and $x = 28$–30 [27]. The $x = 17$–19 alloys are more favorable for future application as magnetostrictive materials because they have similar magnetostriction and contain less costly gallium. Therefore, $Fe_{83}Ga_{17}$ and $Fe_{81}Ga_{19}$ compositions were selected to investigate the microstructure and properties in this work.

It is well known that the morphology of the solid-liquid interface plays a key role in crystal growth during directional solidification. A convex interface (for the vertical Bridgman method, the liquid phase is above and the solid phase below) is beneficial to weed out misoriented crystal grains and it is usually adopted for single-crystal growth [49]. A concave interface will induce chaotically directed growth and this leads to randomly orientation material [50]. A planar interface allows the grains to grow stably and maintain their orientation. Moreover, the chemical composition can be homogeneous over the cross-section surface [49,50]. Therefore, controlling the liquid-solid interface is the key to obtaining a ⟨100⟩ preferred orientation in $Fe_{100-x}Ga_x$ ($x = 17, 19$) DS rods. In order to forecast the thermal profiles and the solid-liquid interface morphology, we used PROCAST to simulate geometries with the rotational symmetry of the casting, as seen in Fig. 2(a). The critical model parameters are summarized in Table I. A unique aspect of the simulation is the use of a location-dependent boundary condition to simulate interaction of the mold with the heater, insulating layer, and coolant. The simulated solid-liquid interface morphologies at withdrawal rates of 25, 3000, and 6000 mm/h are shown in Fig. 1(b). The interface remains planar at withdraw rates of up to 3000 mm/h, and changes to concave at 6000 mm/h. According to solid-liquid interface morphologies, the crystal-growth process can be simulated as shown in Fig. 1(c). For the first two rods in Fig. 2, the interface advances with a planar morphology, while the interface gradually becomes more concave during growth in the last rod. The followed experiments also support these results.

The predicted distribution of temperature during the DS process is shown in Fig. 2(d). The shape of the isothermal lines is consistent with the solid-liquid interface morphology. They are straight for withdrawal rates of 25 and 3000 mm/h, and concave for withdrawal at 6000 mm/h. The solidification rate (V) can be calculated from the withdrawal rate (R) and the temperature gradient (G_L) near the solid-liquid interface by [45,50,51]

$$V = R\,G_L, \tag{1}$$

where G_L is obtained from the temperature field distribution results in Fig. 2(d). The solidification rate V at different withdrawal rates is summarized in Table II. The solidification rate at 25 mm/h is only ~0.8 K/s, which is close to the rate of cast processing. When the withdrawal rate exceeds 3000 mm/h, the solidification rate can reach 100 K/s and it enters the region of subrapid directional solidification [45]. An increase of V may lead to a higher content of dissolved Tb and improves the magnetostrictive performance in the Tb-doped FeGa alloys [40,41,43,45,52].

In order to verify the simulation results, $(Fe_{83}Ga_{17})_{99.9}Tb_{0.1}$ DS rods (without a FeGa ⟨100⟩ seed at the bottom) were prepared at withdrawal rates of 25, 500, 1500, 3000, and 6000 mm/h. Another rod with the same chemical composition was prepared by arc melting and subsequent

TABLE I. Model parameters for solidification modeling [48].

Thermophysical properties	
Liquidus temperature	1750 K
Solidus temperature	1700 K
Rod thermal conductivity	80 W m^{-1} K^{-1}
Mold thermal conductivity	2.5 W m^{-1} K^{-1}
Interface heat transfer coefficients	
Rod mold	200 W m^{-2} K^{-1}
Mold heater	0 (emissivity = 0.4)
Mold insulating layer	500 W m^{-2} K^{-1}
Mold coolant	4000 W m^{-2} K^{-1}
Run parameters	
FE mesh size	0.5 mm
Nodes	542539

TABLE II. Simulated temperature gradient and calculated cooling rate at different withdrawal rates.

Withdrawal rate (mm/h)	Temperature gradient (K/mm)	Cooling rate (K/s)
25	109.4	0.8
3000	129.6	108.1
6000	128.1	213.5

casting into the copper mold without DS for comparison. Microstructural images of these rods are shown in Fig. 3. Figures 3(a)–3(e) show the macrostructural morphology of longitudinal sections of the rods observed in the optical microscope. For the as-cast rod, the fine grains grow towards the edge of the rod because the latent heat is mainly dissipated through the cold copper mold during solidification. The as-cast rod is generally isotropic and no preferred orientation can be achieved. For the rod grown at 25 mm/h, only one large grain and almost no grain boundaries can be seen in the longitudinal section surface, which suggests that the solid-liquid interface is absolutely planar and the specimen grows stably to be almost single crystal. When the withdrawal rate increases to 500 mm/h, several straight columnar grains are observed, indicating quite stable growth but some interfacial instability. The columnar grains are mostly at inclined angles to the growth direction, and the ones with suitable crystallographic orientations can grow significantly in the columnar region. When the withdrawal rate reaches 3000 mm/h, the morphology of columnar grains is retained but the grains are refined and more crooked compared with those in the 500 mm/h rod. However, when the withdrawal rate is doubled to 6000 mm/h, the morphology of columnar grains is thoroughly destroyed and fine grains are distributed over the longitudinal section surface. Stable crystal growth cannot be achieved in this case. The optical morphology above agrees with the simulated results, indicating that the choice of parameters in the PROCAST simulations is reasonable.

The evolution of microstructure and crystal orientation are analyzed through backscattered electron (BSE) images and x-ray diffraction (XRD) patterns, respectively. Figures 3(f)–3(h) shows the BSE images of the as-cast alloy and the cross-section surface of DS rods grown at 25 and 3000 mm/h. For the as-cast alloy, white precipitates are distributed inside the grains and along the grain boundaries. These precipitates possess a hexagonal Th_2Zn_{17}-type crystal structure with space group *Rm* [29,53]. For the DS rods, both volume fraction and precipitate size decrease significantly compared with the as-cast rod. The precipitates are dispersed throughout the rods. The average size and volume fraction of precipitates are summarized in Fig. 3(i). The former decreases from ∼0.9 to below 0.4 μm when the withdrawal rate is increased from 25 to 6000 mm/h, and the latter decreases from approximately 0.12% to 0.08%. Excellent mechanical properties require small, well-dispersed precipitates [45,52], while improved magnetostriction demands more solid solution of Tb [45,54]. The evolution of average size and volume fraction of precipitates indicated by the BSE images may therefore lead to a simultaneous improvement in structural and functional properties.

XRD patterns of the cross-section surfaces of the rods are shown in Fig. 4(a). The diffraction peaks can be indexed in the body-centered-cubic A2 structure for all the specimens. Although the A2 and $D0_3$ phases can both be formed according to the previous studies and have similar body-centered-cubic (bcc) lattice structures [27,55,56], our TEM confirms the A2 structure of the matrix for all of the alloys in this work (Sec. III D1). No additional diffraction peaks can be observed since the size and volume fraction of precipitates is extremely small. With increasing solidification rate, the ⟨200⟩ diffraction peak of the A2 matrix gradually shifts to lower angles [as shown in the enlarged figure in Fig. 4(a)], indicating an increase in lattice parameter. The chemical compositions of both matrix and precipitates determined by EPMA confirm that the compositions of the two phases stabilize around $Fe_{83}Ga_{17}$ and $Fe_{60}Ga_{30}Tb_{10}$ and that their compositions do not depend on the withdrawal rate. Since the composition of the matrix remains almost unchanged, the shift of the ⟨200⟩ peak suggests that more Tb atoms are dissolved in the matrix, in accordance with the reduced volume fraction of precipitates shown in Fig. 3(i). So increasing the withdrawal rate is an effective method to improve the solid solubility of Tb. Here the diffraction peak intensity ratio I_{110}/I_{200} is used to evaluate the degree of ⟨100⟩ orientation because ⟨110⟩ and

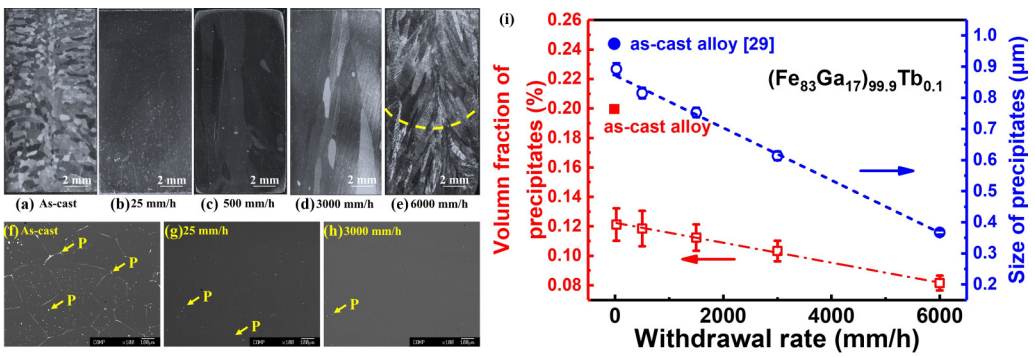

FIG. 3. (a)–(e) Macrostructure of the longitudinal section surface for as-cast and DS $(Fe_{83}Ga_{17})_{99.9}Tb_{0.1}$ rods; the dashed line in (e) indicates the shape of the solid-liquid interface during the DS process. (f)–(h) Backscattered electron images of the cross-section surface for as-cast and DS $(Fe_{83}Ga_{17})_{99.9}Tb_{0.1}$ rods: (f) as-cast, (g) $R = 25$ mm/h, and (h) $R = 3000$ mm/h. (i) The withdrawal rate function of the average size and volume fraction of the Tb-rich precipitates in DS $(Fe_{83}Ga_{17})_{99.9}Tb_{0.1}$ rods.

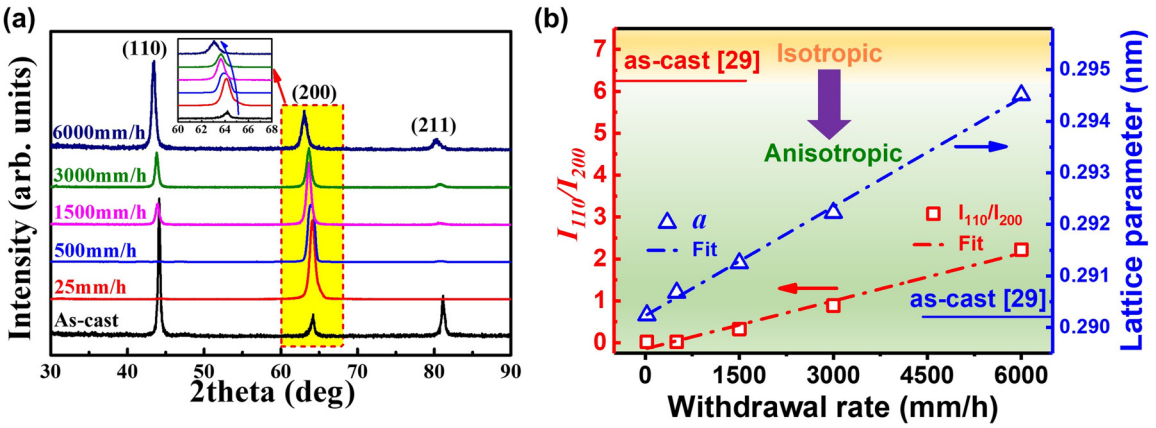

FIG. 4. (a) Room temperature x-ray diffraction patterns of the cross-section surface for as-cast and DS $(Fe_{83}Ga_{17})_{99.9}Tb_{0.1}$ rods. The inset in (a) shows the enhancement of the (200) peak in the range $2\theta \sim 60°$–$68°$. (b) The withdrawal rate dependence of intensity ratio I_{110}/I_{200} and the lattice parameter a for $(Fe_{83}Ga_{17})_{99.9}Tb_{0.1}$ DS rods.

⟨200⟩ are the two main A2 diffraction peaks in $Fe_{100-x}Ga_x$ ($x = 17, 19$). The dependence of the peak intensity ratio and lattice parameter a on the withdrawal rate is summarized in Fig. 4(b). The lattice parameter exhibits a linear increase due to the linear relation between withdrawal rate and solid solubility of Tb. The I_{110}/I_{200} ratio also increases linearly with withdrawal rate, indicating gradual deterioration of the ⟨100⟩ orientation. For the rods grown at 3000 mm/h or less, the ratio is less than 1, indicating that ⟨100⟩ orientation is preferred. When the withdrawal rate increases to 6000 mm/h, the columnar grain morphology disappears so the I_{110}/I_{200} value increases significantly but it remains three times less than that of the as-cast rod, which is marked by the red solid line in Fig. 4(b). The $(Fe_{83}Ga_{17})_{99.9}Tb_{0.1}$ rods prepared by DS are anisotropic despite quite different grain morphologies, and a significant ⟨100⟩ preferred orientation can be realized in an appropriate processing range.

The magnetostrictive properties of the as-cast and DS rods were measured along the longitudinal direction using the standard strain gauge method. Optimal magnetostriction requires several tens of MPa precompressive stress to initialize the magnetic domain state (this is called the stress effect on magnetostriction) [30,57,58]. Here we measured magnetostriction in the stress-free condition and under 30 MPa, as shown in Figs. 5(a)–5(f). A summary of magnetostriction is provided in Fig. 5(g), where three regions, i.e., (I) enhanced region, (II) stable region, and (III) declining region, are indicated by different colors. In region I, the excellent ⟨100⟩ orientation and increasing Tb solid solubility lead to a significant increase of magnetostriction from ∼160 to ∼220 ppm. In region II, more Tb is dissolved in the matrix and it improves the magnetostriction further, but the ⟨100⟩ orientation is gradually degraded. These opposite influences stabilize the magnetostriction here at around 215 ppm. In region III, the destruction of ⟨100⟩ orientation sharply reduces the magnetostriction to ∼100 ppm.

We find that the ⟨100⟩ orientation can be improved by placing a ⟨100⟩ single-crystal seed at the bottom of the master rod during DS, providing the grains maintain a stable axial growth (this method is called SDS). A withdrawal rate of 3000 mm/h [as marked by the arrow in Fig. 5(g)] is considered to be optimal to prepare FeGa-Tb magnetostrictive rods with a seed crystal because the Tb solubility is largest, with relatively good ⟨100⟩ orientation.

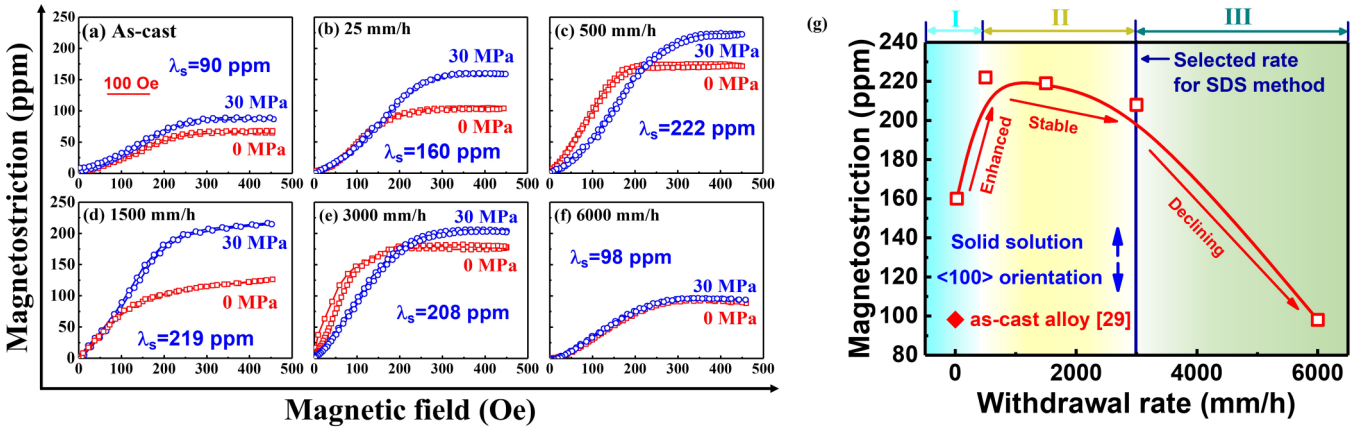

FIG. 5. (a)–(f) Measured magnetostriction curves under the stress-free condition and under compressive stress of 30 MPa for as-cast and DS $(Fe_{83}Ga_{17})_{99.9}Tb_{0.1}$ rods. (g) The withdrawal rate dependence of the largest measured magnetostriction.

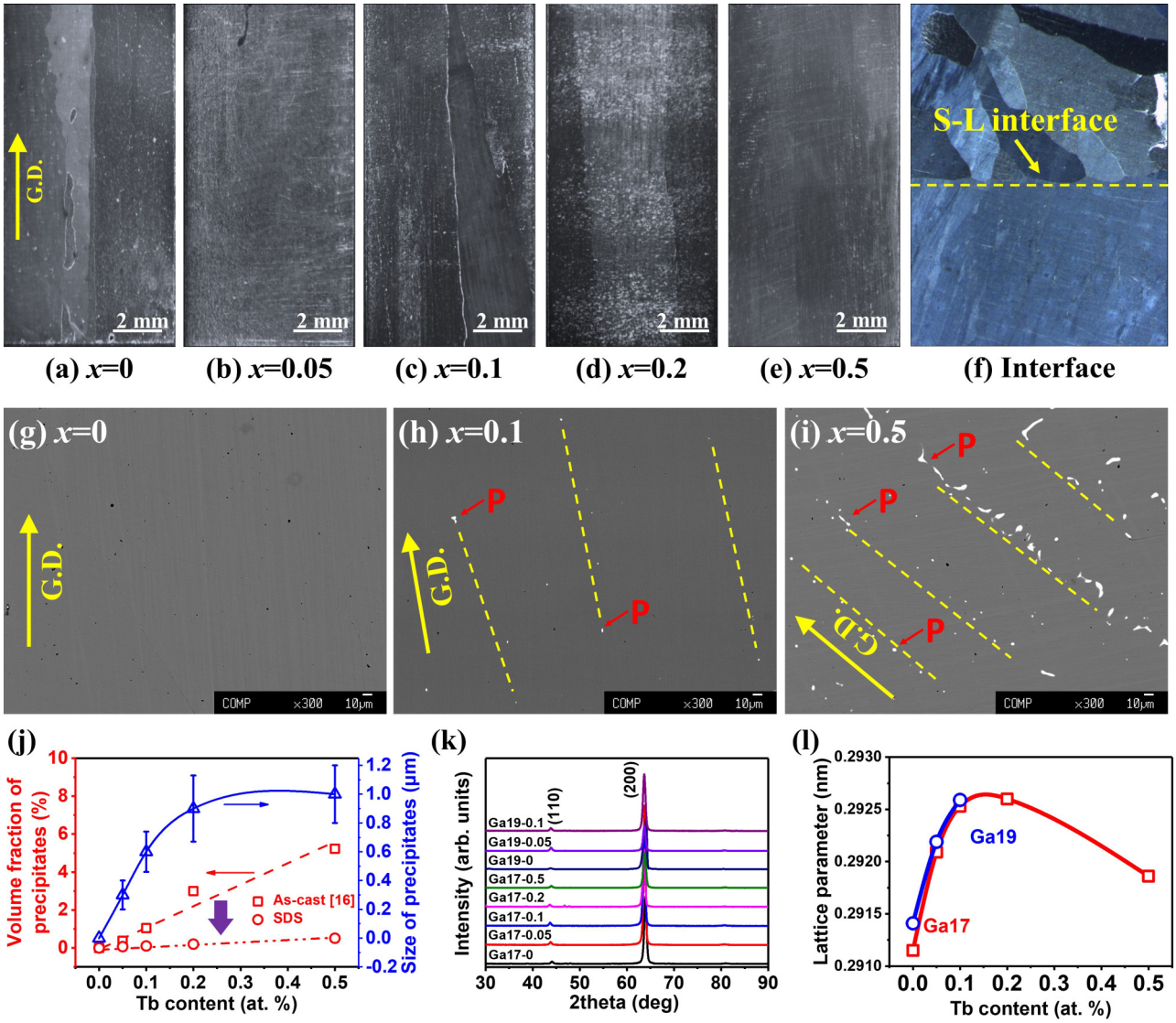

FIG. 6. (a)–(e) Macrostructure of the longitudinal section surface for $(Fe_{83}Ga_{17})_{100-x}Tb_x$ SDS rods. (f) The morphology of the solid-liquid interface of the SDS $(Fe_{83}Ga_{17})_{99.9}Tb_{0.1}$ rod. (g)–(i) Backscattered electron images of the longitudinal section surface for $(Fe_{83}Ga_{17})_{100-x}Tb_x$ SDS rods with (g) $x = 0$, (h) $x = 0.1$, and (i) $x = 0.5$, respectively. (j) Tb content dependence of volume fraction and average size of precipitates for $(Fe_{83}Ga_{17})_{100-x}Tb_x$ and $(Fe_{81}Ga_{19})_{100-x}Tb_x$ SDS rods; the average size of precipitates for as-cast rods with the same Tb concentrations is also exhibited in (j) for comparison. (k) Room-temperature x-ray diffraction patterns for $(Fe_{83}Ga_{17})_{100-x}Tb_x$ ($x = 0$–0.5) and $(Fe_{81}Ga_{19})_{100-x}Tb_x$ ($x = 0-0.1$) SDS rods with the x rays incident on the cross-section surface. The inset shows the evolution of the lattice parameter with the Tb content of the SDS rods.

B. Microstructure of SDS FeGa-Tb alloys

Rods of two FeGa alloys systems: $(Fe_{83}Ga_{17})_{100-x}Tb_x$ ($x = 0, 0.05, 0.1, 0.2, 0.5$) and $(Fe_{81}Ga_{19})_{100-x}Tb_x$ ($x = 0, 0.05, 0.1$), are prepared by the SDS method. For convenience, the alloys are denoted as Ga17-x and Ga19-x, where x expresses the percentage of Tb atoms.

Figures 6(a)–6(e) shows the macromorphologies of the longitudinal section of Ga17-x ($x = 0$–0.5) SDS rods grown at 3000 mm/h. Obviously, straight columnar grain morphologies are observed for all of them, whatever the Tb content. The Tb concentration does not change the crystal-growth process. The morphology of the solid-liquid interface is frozen by rapid quench at the rate of 72000 mm/h (2×10^4 μm/s), and the interface morphology of an $x = 0.1$ rod is illustrated in Fig. 6(f). The lower part shows the columnar grains formed during the SDS process, and the upper part is the master rod. The solid-liquid interface marked by the yellow dashed line is obviously planar. Similar grain morphologies are observed in Ga19-x ($x = 0$–0.1) rods. The planar interface provides the opportunity for stable crystal growth.

BSE images in Figs. 6(g)–6(i) show the longitudinal sections of Ga17-0, Ga17-0.1, and Ga19-0.5 rods. For the binary alloy, a single-phase microstructure is confirmed by the homogeneous color of the image. When a small amount of Tb is added, dispersive Tb-rich precipitates in the submicron-size range are formed in the A2 matrix. With the increasing concentration of Tb, the volume fraction and size of the precipitates increase. Figure 6(j) summarizes their Tb

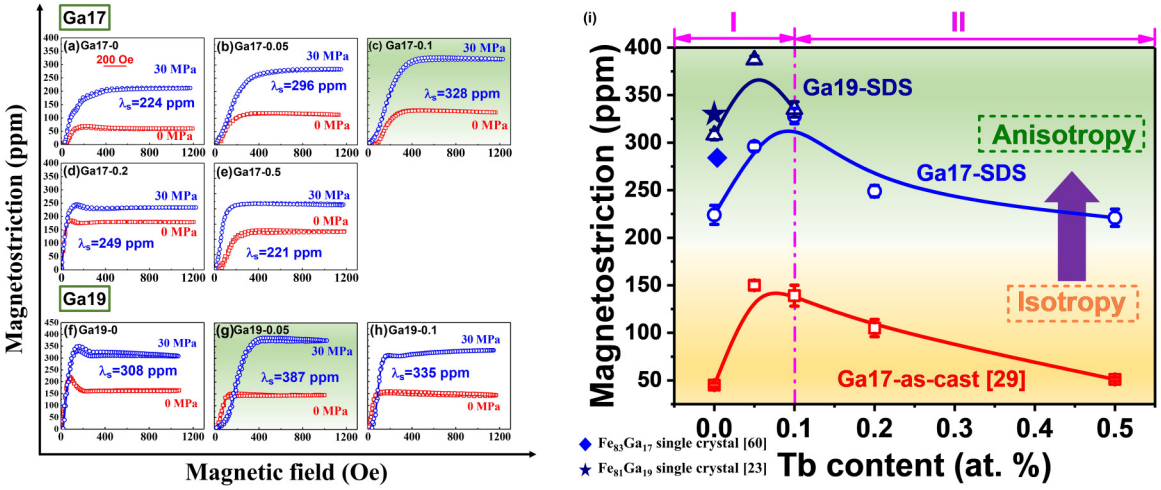

FIG. 7. (a)–(h) Measured magnetostriction curves under the stress-free condition and the compressive stress of 30 MPa for $(Fe_{83}Ga_{17})_{100-x}Tb_x$ ($x = 0-0.5$) and $(Fe_{81}Ga_{19})_{100-x}Tb_x$ ($x = 0-0.1$) SDS rods. (i) Tb content function of largest measured magnetostriction for as-cast $(Fe_{83}Ga_{17})_{100-x}Tb_x$ ($x = 0$–0.5) alloys (the data is from Ref. [29]), SDS $(Fe_{83}Ga_{17})_{100-x}Tb_x$ ($x = 0$–0.5) rods, and SDS $(Fe_{81}Ga_{19})_{100-x}Tb_x$ ($x = 0 - -0.1$) rods. The magnetostriction of $Fe_{83}Ga_{17}$ and $Fe_{81}Ga_{19}$ single crystals is also exhibited; data is extracted from Refs. [60] and [23], respectively.

dependence, and they are compared with those in as-cast alloys from Ref. [29]. The precipitate size exhibits a positive correlation with Tb content, and finally settles at approximately 1.0 μm when x exceeds 0.5. The volume fraction of precipitates in SDS rods and as-cast alloys both exhibit a linear relation with Tb content. Although traces of Tb can enter the lattice, the solid solubility can never be great due to the large difference in atomic radius between Tb and Fe or Ga. The vast majority of the Tb forms Tb-rich precipitates, so the volume fraction of precipitates has a linear relation with Tb content. The remarkable reduction of the volume fraction suggests that more Tb atoms are in solution in the SDS rods compared with the as-cast alloys while the overall chemical composition remains unchanged, due to the higher solidification speed of the SDS method. Moreover, the precipitates basically distribute along the crystal-growth direction, which is marked by the yellow arrows in Figs. 6(h) and 6(i). The reasons are discussed in Sec. III D 2. XRD patterns of the cross section are performed to analyze the crystal orientation and lattice parameters. All the Ga17 and Ga19 SDS rods possess a satisfactory ⟨100⟩ orientation since (200) is the only prominent diffraction peak and the (110) and (211) peak intensities are almost negligible. The crystal lattice expands in Tb-doped rods compared with Tb-free rods in both Ga17 and Ga19 alloy systems, as shown in Fig. 6(l).

In summary, the microstructural analysis has proved that highly ⟨100⟩-orientated FeGa-Tb rods can be prepared by placing a ⟨100⟩ seed on the bottom of the master rods and setting the withdrawal rate at 3000 mm/h. Fine precipitates with submicron sizes are formed by trace Tb addition, and they distribute dispersively parallel to the crystal-growth direction.

C. Magnetostrictive and tensile mechanical properties of SDS FeGa-Tb alloys

Figures 7(a)–7(h) shows the magnetostrictive measurement curves for Ga17 and Ga19 SDS rods along the growth direction in the free state and under the precompressive stress of 30 MPa. Here we only compare the maximum magnetostriction actually measured rather than the 1.5 times of the measured magnetostriction in the stress-free state because the initial direction distribution of magnetic domains is random and the measured maximum magnetostriction under precompressive stress is always lower than the calculated value [27,45,59]. For practical applications, it is the measured magnetostriction that counts, which is the one we choose to compare. The Tb dependence of magnetostriction measured under 30 MPa is summarized in Fig. 7(i); the corresponding values for a $Fe_{83}Ga_{17}$ single crystal [60], a $Fe_{81}Ga_{19}$ single crystal [23], and $(Fe_{83}Ga_{17})_{100-x}Tb_x$ as-cast alloys [29] are also marked in the figure in order to make the comparison. On transformation from an isotropic system (as-cast alloys) to an anisotropic system (SDS rods), the magnetostriction undergoes a remarkable improvement, establishing the benefit of seeded directional solidification. The magnetostriction reaches 224 and 308 ppm in the binary $Fe_{83}Ga_{17}$ and $Fe_{81}Ga_{19}$ orientated rods, respectively. The two values are close to that of a binary ⟨001⟩ single crystal with the same chemical composition [23,60], showing that the existence of grain boundaries parallel to the growth direction does not decrease the performance significantly. When traces of Tb are doped into the FeGa alloys, magnetostriction reaches 328 and 387 ppm for the Ga17-0.1 rod and the Ga19-0.05 rod, respectively. These values are higher than the binary single crystals, but beyond a certain Tb content, the magnetostriction starts to fall off.

We mentioned in Sec. I that FeGa binary alloys are brittle solid solutions, where the tensile fracture strain can reach only ∼0.3% [18,29] and 2% [22], respectively, for as-cast polycrystalline and single-crystal samples. In previous work, we discovered that an appropriate density and morphology of Tb-rich precipitates can significantly improve the tensile fracture strain in as-cast FeGa magnetostrictive alloys as the material transforms from a brittle single-phase alloy to a

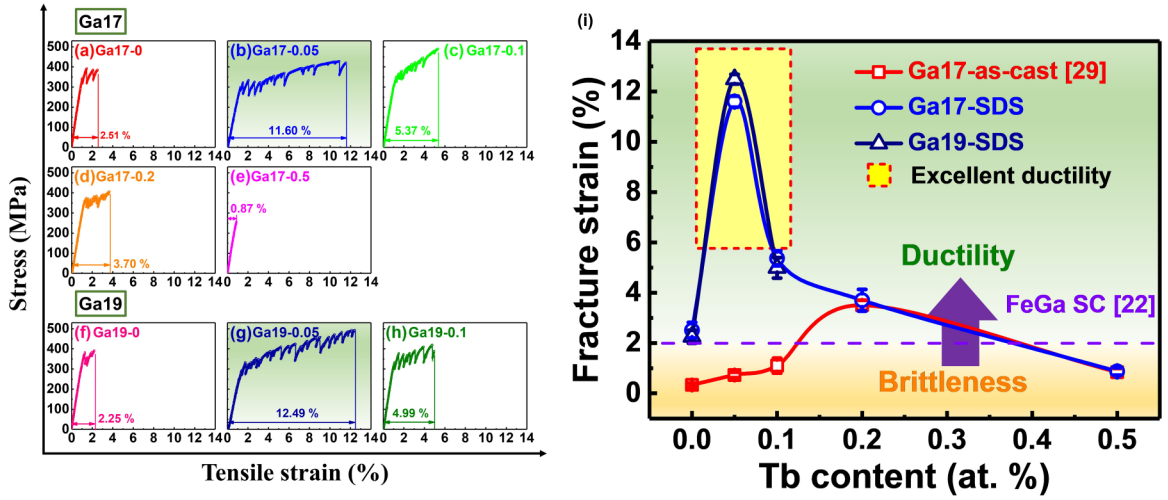

FIG. 8. (a)–(h) Tensile stress-strain curves for $(Fe_{83}Ga_{17})_{100-x}Tb_x$ ($x = 0$–0.5) and $(Fe_{81}Ga_{19})_{100-x}Tb_x$ ($x = 0$–0.1) SDS rods measured at room temperature. (i) Tb content function of tensile fracture strain for as-cast $(Fe_{83}Ga_{17})_{100-x}Tb_x$ ($x = 0$–0.5) alloys (the data is from Ref. [29]), SDS $(Fe_{83}Ga_{17})_{100-x}Tb_x$ ($x = 0$–0.5) rods, and SDS $(Fe_{81}Ga_{19})_{100-x}Tb_x$ ($x = 0$–0.1) rods. The tensile fracture strain of a binary single crystal is exhibited by the dashed line; the data is extracted from Ref. [22].

ductile dual-phase alloy [38,52]. Here, the tensile measurements are performed for all the rods along the ⟨100⟩ direction. Figures 8(a)–8(h) shows the tensile stress-strain curves of all the Ga17 and Ga19 directionally solidified specimens, and the corresponding fracture strains are indicated below each curve. Plastic behavior appears in most specimens except Ga17-0.5. However, a zigzag shape is seen in the plastic range which is different from the as-cast FeGa(-Tb) alloys [29]. The reason is discussed later. Since the yield strength and ultimate tensile strengths for all the specimens are concentrated around ∼300–350 MPa and ∼400–450 MPa, respectively, only the fracture strain of each specimen is summarized and compared with the as-cast alloys in Fig. 8(i). For Ga17 and Ga19 SDS rods, the fracture strains are almost equal for as-cast alloys and SDS rods when the Tb addition is the same. The fracture strain for the binary oriented rods is just over 2%, which is close to the performance of the binary single crystal [22,61]. When a little Tb is added into the binary system, the fracture strain shifts up to over 10%, accompanied by the formation of submicron-sized precipitates. The 12.5% strain obtained in the Ga19-0.05 SDS rod is over 40 times larger than that in the binary as-cast alloy. At a Tb content of 0.1 at.%, the fracture strain is still over 5% and the ductility of SDS rods is significantly superior to that of as-cast alloys. However, with further increase of Tb content, the fracture strain falls sharply and the values almost overlap with the as-cast alloys. In Fig. 8(i), a purple dashed line marks brittleness and ductility, which correspond to the tensile fracture strain of a FeGa single crystal [22]. Obviously, the SDS method broadens the range of Tb content for high ductility. Moreover, the yellow block, which denotes the ductile region, surrounds the performance peak for SDS rods. Here the superb tensile fracture strain is quite enough for further processing and regular operation under pressure. Our results indicate that an appropriate density of precipitates is good for ductility and the best tensile properties.

D. Discussion

From Figs. 7(i) and 8(i), it can be seen that the magnetostriction and ductility of FeGa-Tb alloys can be simultaneously optimized when the Tb concentration is around 0.05–0.10 at.%. For the Ga19-0.05 alloy, the magnetostriction and tensile fracture strain reach 387 ppm and 12.5%, respectively. Therefore, we have a practical magnetostrictive material with minimal RE content, which offers a remarkable combination of structure and function that opens the prospect of widespread applications. Two main issues are now discussed:

(1) Why is the magnetostriction improved when traces of Tb are added in the SDS rods?

(2) Why is ductility so large in the Tb-doped SDS rods?

In order to answer these questions, we have investigated the crystal structure and phase structure in detail to understand the relevant microstructural factors.

1. Mechanism for improved magnetostriction

According to the metastable binary Fe-Ga phase diagram [62], both A2 and $D0_3$ phases are expected to appear in $Fe_{83}Ga_{17}$ and $Fe_{81}Ga_{19}$ alloys. Recent investigations have established that modified-$D0_3$ ($L6_0$ structure) nanoinclusions may also exist in the matrix, and the enhanced magnetostriction of FeGa is now believed to originate from a tetragonal distortion in the matrix induced by these modified-$D0_3$ nanoinclusions [43,63–67]. The lattice structures of the three phases are shown in Figs. 9(a)–9(c). The A2 phase has a body-centered-cubic (bcc) structure with randomly distributed Ga atoms, while the Ga atoms in the cubic $D0_3$ phase have a preferred occupation site along two perpendicular ⟨110⟩ directions. The modified-$D0_3$ phase has a tetragonal structure with two Ga-Ga nearest-neighbor pairs distributed along the same ⟨001⟩ direction [43]. Even so, the lattice parameters of the three phases are very close, so they are difficult to distinguish by XRD. We have confirmed by TEM analysis that

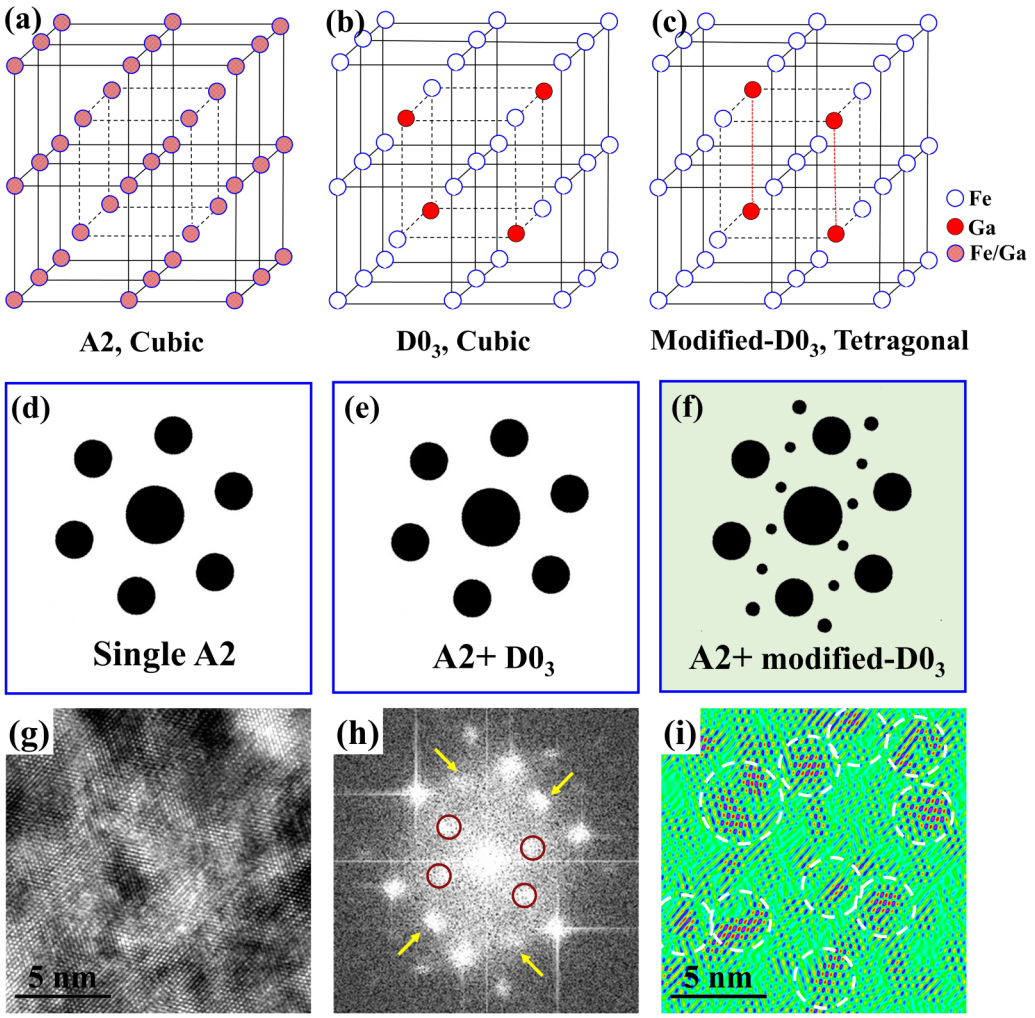

FIG. 9. (a)–(c) Lattice structures for (a) A2 phase, (b) $D0_3$ phase, and (c) modified-$D0_3$ phase with the composition of Fe_3Ga. (d)–(f) Simulated electron diffraction pattern viewing from the ⟨111⟩ direction for (d) single A2 phase, (e) mixture of A2 phase and $D0_3$ phase, and (f) mixture of A2 phase and modified-$D0_3$ phase. (g) High-resolution electron microscopy morphology of the Ga19-0.05 SDS alloy viewed from the ⟨111⟩ direction. (h) The corresponding fast Fourier transform (FFT) pattern for the region in (g). (i) The inverse fast Fourier transform (IFFT) figure obtained by using the four weak ⟨011⟩ superlattice reflections as a mask to filter the HREM image in (h).

it is the tetragonally modified-$D0_3$ phase rather than the cubic $D0_3$ phase that coexists with the A2 matrix. In Fig. 10(a), the selected area electron diffraction (SAED) pattern of [100] zone axis for the binary Ga19-0 alloy shows a clear characteristic of a single A2 structure marked by the absence of superlattice spots in the patterns. When doping with Tb, superlattice spots appear in the SAED pattern, as shown in the inset of Fig. 10(d). This means that an ordered phase appears in the alloy. Two pieces of evidence prove it is the modified-$D0_3$ phase rather than the cubic $D0_3$ phase. First, the cubic phase exhibits relatively negative magnetostriction along the ⟨100⟩ directions [46], so its presence should degrade magnetostriction of FeGa alloys rather than enhance it, as is the case with 0.05 at.% Tb dopant (20% increase). Second, the electron diffraction patterns for A2 + $D0_3$ and A2 + modified-$D0_3$ phases are significantly different when viewed along the ⟨111⟩ direction. The simulated diffraction patterns are shown in Figs. 9(d)–9(f), and is compared with the experimental results in Fig. 9(h). No superlattice diffraction spots should appear for the A2 + $D0_3$ phases, while ⟨011⟩-type superlattice reflections will appear when A2 and modified-$D0_3$ phases coexist. High-resolution TEM images and the corresponding fast Fourier transform (FFT) spectrum along ⟨111⟩ are used to confirm the phases, as shown in Figs. 9(g) and 9(h). Obviously, the FFT result is in accordance with Fig. 9(f), indicating the coexistence of the A2 phase and modified-$D0_3$ inclusions. The absence of the $D0_3$ phase is attributed to the rapid cooling rate during the SDS process. Since the size of modified-$D0_3$ inclusions is generally less than 10 nm, the lattice parameter difference between A2 and modified-$D0_3$ phases is tiny, so it is difficult to recognize the location and distribution of modified-$D0_3$ inclusions without the inverse FFT analysis shown in Fig. 9(i). Four weak ⟨011⟩ superlattice reflections resulting from the modified-$D0_3$ inclusions are used as a mask to filter the HREM image; therefore, the areas with high intensities (shown by blue and red color in the figures) in the inverse fast Fourier transform image clearly show the positions of the modified-$D0_3$ inclusions, as presented by the white circles in Fig. 9(i). Figure 9(i) is similar to the dark-field image; the homogeneous green color

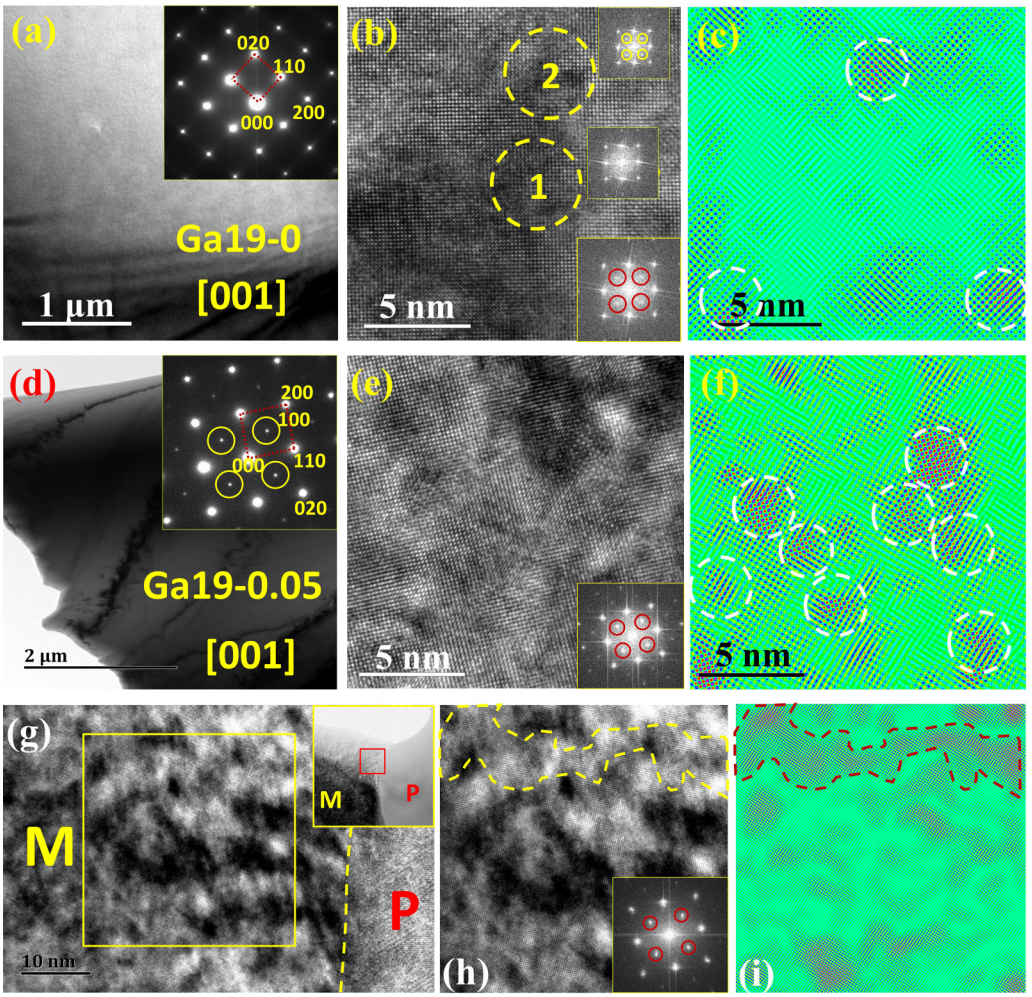

FIG. 10. (a)–(c) TEM image, HRTEM image, and IFFT patterns of Ga19-0 SDS rod. (d)–(f) TEM image, HRTEM image, and IFFT patterns of the Ga19-0.05 SDS rod. (g)–(i) HRTEM images and IFFT patterns of matrix nearby a precipitate in the Ga19-0.05 SDS rod.

means no contribution to the ⟨011⟩-type superlattice spots selected as masks for the inverse FFT image. Therefore, the IFFT image can effectively reflect the size and distribution of modified-$D0_3$ inclusions, as marked by the dotted white circles in Fig. 9(i).

The modified-$D0_3$ inclusions are tetragonally distorted along a ⟨001⟩ direction, so the TEM images are next viewed along [001]. The difference is the appearance of ⟨001⟩-type superlattice spots in Fig. 10(d) but the absence in Fig. 10(a), which is associated with the addition of Tb. For the HREM image of Ga19-0 alloy in Fig. 10(b), the FFT spectrum of region 1 shows no superlattice reflection, but the FFT spectrum of region 2 shows the appearance of superlattice reflections. The FFT spectrum of the whole region in Fig. 10(b) is placed at the bottom right where weak superlattice spots can be observed overall. In contrast, more intense superlattice spots appear in the corresponding FFT spectrum of the whole region in Fig. 10(d) for Ga19-0.05 alloy. This suggests a higher density of modified-$D0_3$ inclusions in the Tb-doped alloy. Four ⟨001⟩ superlattice reflections are again used as a mask to get the inverse FFT images based on the HREM images. Figures 10(c) and 10(f) compare the distribution of modified-$D0_3$ inclusions between Ga19-0 and Ga19-0.05 alloys. The density of modified-$D0_3$ inclusions increases with traces of Tb addition. Note that Figs. 9 and 10 are typical data selected from more than 20 areas.

The magnetostriction in $Fe_{100-x}Ga_x$ ($x = 17, 19$) alloys is thought of as a reflection of the tetragonal distortion in the A2 matrix induced by the dispersion of tetragonal modified-$D0_3$ inclusions [42,43]. The induced deformation of the A2 matrix can be reoriented without hysteresis in a small magnetic field, suggesting vanishing structural anisotropy. Simultaneously, there is a single-ion crystal field contribution related to the Tb quadrupole moment Q, which can also contribute to the magnetostriction [34]. In this work, despite the limited solidification speed in the SDS method compared to melt spinning, some Tb atoms are nevertheless dissolved in the A2 matrix. This produces a higher density of modified-$D0_3$ inclusions in the matrix than the undoped alloys, resulting in larger local strains, so the magnetostriction is enhanced. Moreover, the microstructure in the matrix containing the submicron precipitates is also investigated, as shown in Figs. 10(g)–10(i). The modified-$D0_3$ inclusions exhibit a bandlike distribution rather than being randomly distributed in the A2 matrix, as marked in Fig. 10(g). The high density of modified-$D0_3$ inclusions in a local region may contribute further to the

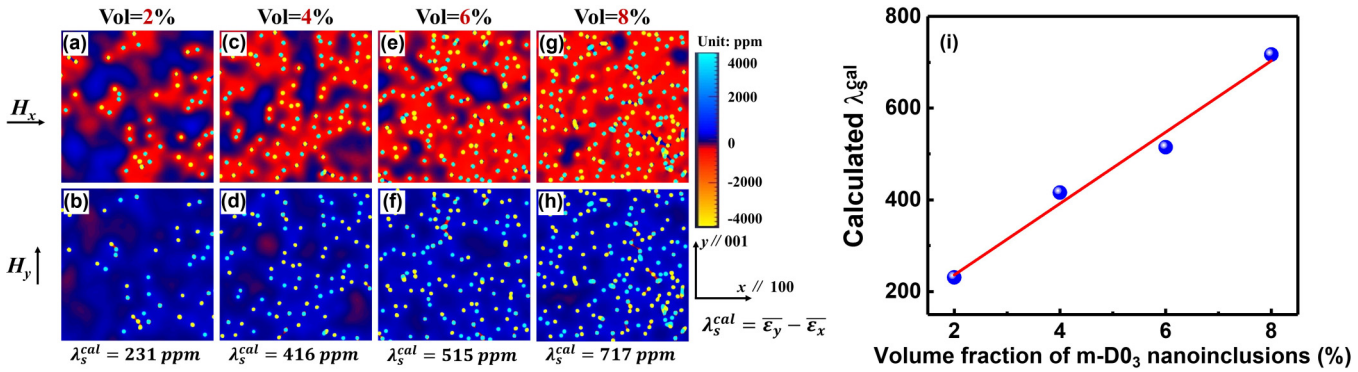

FIG. 11. Two-dimensional (2D) phase-field simulations illustrating the relationship between modified-D0$_3$ nanoinclusion concentration and magnetostriction. (a)–(h) The strain distribution under horizontal magnetic field (||100) and under vertical magnetic field (||001); the calculated saturation magnetostriction is on the bottom of the figures. (i) The calculated λ_s^{cal} vs the volume fraction of modified-D0$_3$ nanoinclusions based on 2D phase-field simulation results.

magnetostriction. The special distribution may be caused by the semicoherent interface between the submicron precipitates and the A2 matrix, as has been shown in our previous investigations [16]. With increasing Tb concentration, the precipitates grow larger so that the semicoherent interface with the A2 matrix transforms to an incoherent interface. The positive effect on magnetostriction disappears and the magnetostriction falls off. In this case, the effect of dissolved Tb atoms is still present, so the magnetostriction for Tb-0.5 at.% doped alloy is approximately equal to that for binary alloys in both isotropic (as-cast alloys) and anisotropic (SDS rods) systems [see Fig. 7(i)].

A two-dimensional phase-field simulation is performed to explain the mechanism where an increasing concentration of modified-D0$_3$ nanoinclusions improves the magnetostriction, as shown in Fig. 11. The spots in Figs. 11(a)–11(h) denote the modified-D0$_3$ nanoclusters; the horizontal and vertical directions represent [100] and [001] directions, respectively. Here, four concentrations of 2%, 4%, 6%, and 8% are simulated. The calculation method of magnetostriction is as follows. First, a horizontal magnetic field is applied along the [100] direction to simulate the condition of applying precompressive strain; then we can obtain a value of $\overline{\varepsilon_x}$. Subsequently, a vertical magnetic field along the [001] direction is applied to simulate the condition of applying a magnetic field to measure the saturation magnetostriction; here we can obtain another value of $\overline{\varepsilon_y}$. Therefore, the calculated saturation magnetostriction should be $\lambda_s^{cal} = \overline{\varepsilon_y} - \overline{\varepsilon_x}$. According to the phase-field simulation results, the calculated saturation magnetostriction λ_s^{cal} increases almost linearly with increasing concentration of modified-D0$_3$ nanoinclusions, from 231 ppm when the concentration is 2% to 717 ppm when the concentration is 8%, as summarized in Fig. 11(i). Therefore, the conclusion that a higher concentration of modified-D0$_3$ nanoinclusions results in larger magnetostriction along the [001] direction is confirmed, in accordance with microstructural observation and magnetic experiments.

2. *Mechanism for improved ductility*

The intrinsic mechanical properties of $Fe_{83}Ga_{17}$ single crystals were described in in Ref. [22]. However, we find that the tensile fracture strain in the Tb-doped alloys is significantly improved. This should be attributed to a change in microstructure. Figures 12(a) and 12(b), respectively, present optical and backscattered electron (BSE) images of the longitudinal section surface in a Ga17-Tb0.5 rod, and the crystal-growth direction in indicated by the white G.D. arrows to the left of each figure. The morphology of columnar grains is observed and the black lines mark the grain boundaries (GBs). Moreover, there are numerous black spots aligned parallel to the growth direction, and these spots are confirmed to be the Tb-rich precipitates according to the BSE image. The average width of a distribution line of the particulate precipitates is 15–20 μm according the optical image and this result is well in line with the BSE image. The reasons for the different shape and distribution of the Tb-rich precipitates in the SDS rods compared with the as-cast alloys are schematically explained by Fig. 12(c). When the withdrawal rate is quite low, the solid-liquid interface is weakly perturbed from a microscale perspective and these result in a cellular structure corresponding to a column grain morphology. The higher the withdrawal rate, the smaller the distance between the adjacent cellular crystals. If the withdrawal rate increases further, the tip of the cellular crystals becomes more pointed, the side walls begin to destabilize, and the cellular grains tend to transfer to dendritic grains. In our previous investigation, the Tb-rich precipitates have been proved to have a melting point ~200 K lower than the matrix [29]. The precipitates solidify after the crystallization of the matrix is completed. The sidewall instability of the cellular crystals just sets in at a withdrawal rate of 3000 mm/h, so there are slight embossments along the walls. The crystal-growth process of the matrix finishes when the embossments of the adjacent cellular crystals join up. At this point, the liquid precipitates are segregated by the embossments, as shown in Fig. 12(c), so the particulate precipitates distribute parallel to the crystal-growth direction. SEM and TEM analyses are performed to understand the mechanism of improvement in ductility due to the Tb.

In the binary as-cast polycrystals, the tensile fracture strain is only ~0.2%–0.3% because cracks propagate rapidly along the grain boundaries, and the fracture surface generally exhibits the features of intergranular fracture [18,29]. The morphology of a fracture surface for the Ga19-0 SDS alloy

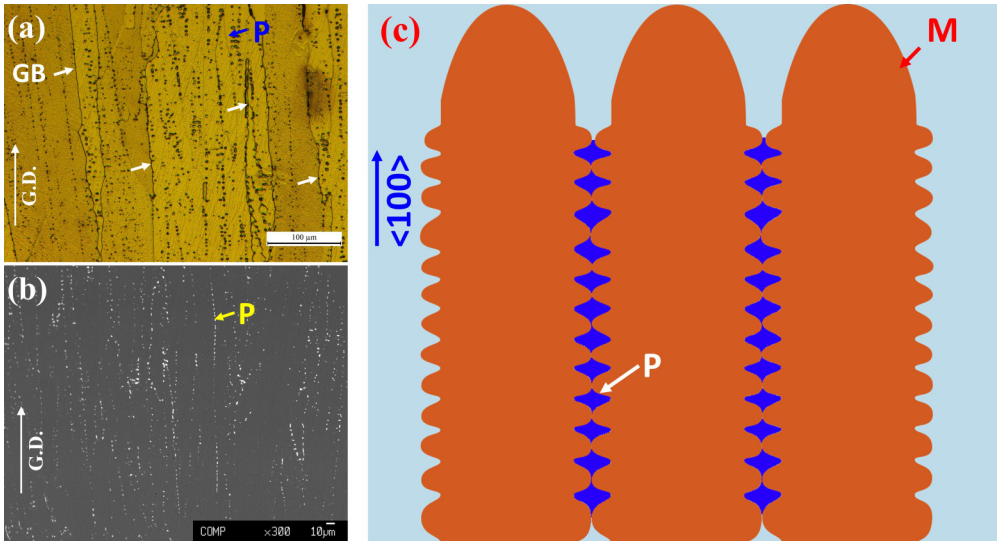

FIG. 12. (a) Optical morphology of the longitudinal section surface for the Ga19-0.05 SDS rod. (b) Backscattered electron image of the longitudinal section surface for a Ga19-0.05 SDS rod. (c) The schematic diagram which explains the special distribution of the Tb-rich precipitates.

is shown in Figs. 13(a) and 13(b). A striking contrast can be observed in that the SDS alloy exhibits characteristic transgranular fracture. The large cracks, marked by red arrows in Fig. 13(a), are the grain boundaries. In each columnar grain, obvious oriented distributed slip bands can be observed, as indicated by the yellow dashed lines. In Fig. 13(b), a tiny steplike morphology can be observed, as indicated by the yellow arrows. That means the main slip bands perpendicular to the tensile direction are activated and they gradually extend during the deformation. The columnar grain cracks when the slip bands move across the grain. However, the grain boundaries perpendicular to the growth direction are eliminated and only a few parallel boundaries exist in the rods, so the cracks cannot pass across the grains through the GBs. Hence the ductility of the binary alloys is improved by SDS processing.

In ∼0.05–1 at.% Tb-doped SDS rods, the submicron Tb-rich precipitates are linearly distributed parallel to the growth direction [Figs. 6(h) and 6(i)]. For these specimens, the height of the steps in the fracture surfaces is significantly larger than that for the binary alloy, as indicated in Figs. 13(c) and 13(d). It is suggested that the particulate precipitates have sharp angles [see Figs. 13(e) and 13(f)] and this easily leads to stress concentration when the grain is deformed because of the incoherence between matrix and precipitates. Therefore, slip bands are preferentially activated nearby the precipitates, and more slip bands in different directions could be developed due to the stress concentration. So the slip bands need to move longer distances to meet and this results in the larger height of the steps and contributes to the ductility. Moreover, fracture requires the dislocations to cross the precipitates. The effect of precipitates is shown in Figs. 13(e) and 13(f), which

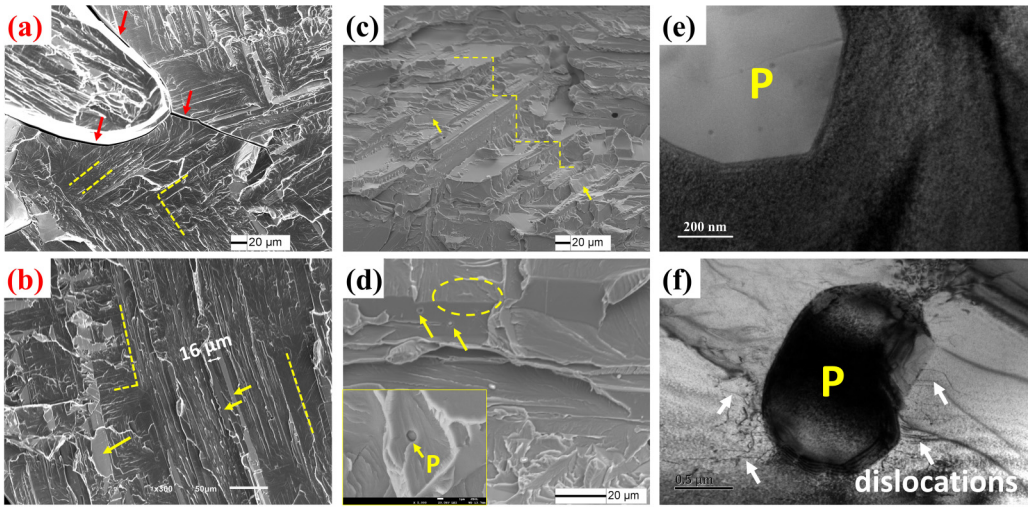

FIG. 13. (a),(b) Fracture surface morphologies of an undoped Ga19-0 SDS rod. (c),(d) Fracture surface morphologies of a Tb-doped Ga19-0.05 SDS rod. (e),(f) TEM images of the matrix nearby a precipitate (e) before tensile test and (f) after tensile deformation of 2%.

are TEM images of the region around a precipitate in the Ga19-0.05 SDS rod. The former TEM specimen is cut from the unstressed rod and the latter one is cut from a tensile test specimen after 3% tensile deformation. In the unstressed rod, no dislocations are observed around the precipitate. After the tensile deformation, a high density of dislocations terminates in the interface between the matrix and the precipitate, and no dislocation is able to reach the precipitate. Therefore, the precipitates effectively hinder crack motion. They are eventually cut through, forming the dimples, indicated by yellow arrows in Fig. 13(d). Besides, the termination and activation of dislocations caused by precipitates can also result in the zigzag shape in tensile stress-strain curves, and the formation of precipitates leads to a further accumulation of dislocations. Therefore, the ductility of the Tb-0.05% and Tb-0.1% SDS rods is significantly better than the binary rods due to the formation of particulate precipitates.

When the size and volume fraction of precipitates is increased by adding more Tb, the tensile fracture strain returns to almost the same value as for the as-cast alloys (see Fig. 8), and the improvement of ductility completely disappears. There may be two reasons. First, increasing precipitate size eliminates the semicoherent relationship with the matrix, so their influence on dislocation motion is weakened. Second, the intrinsic brittleness of the precipitates means that they are sources of microcracks, and the high density of precipitates can generate a fast track for the cracks to cross the tensile specimen. Therefore, a combination of perfect columnar grain morphology with appropriate density and size of precipitates is needed for optimal ductility in FeGa-Tb magnetostrictive alloys.

E. Summary and outlook

We have shown that the Tb-doped SDS rods combine significantly improved saturation magnetostriction and tensile fracture strain as compared to the other solid solutions summarized in Sec. I. This offers the possibility of changing the shape of the FeGa alloys by rolling or swagging to form sheets or wires, thereby enlarging the range of magnetostrictive applications. We were able to roll the Tb-0.05 at.% SDS rod and found that it can be easily reduced to a sheet with the thickness of 0.1 mm or even less. Sheets of FeGa alloys with traces of Tb may now be able to replace more conventional magnetostrictive materials such as some metallic glasses, other Fe/Ni-based alloys, and Tefernol-D in applications such as nondestructive testing of high-speed steel rails or ultraprecise position control [68–70].

The comparison of the measured magnetostriction and tensile fracture strain of the Fe-based magnetostrictive materials and Terfenol-D was shown in Fig. 1 The materials in region I show quite low magnetostriction, but those in region II have satisfactory magnetostriction but limited ductility. The $Fe_{82}Ga_{13.5}Al_{4.5}$ rod of Ref. [21] and the $(Fe_{81}Ga_{19})_{99.5}Tb_{0.05}$ SDS rod of the present work (region III) show a combination of outstanding magnetostriction and excellent tensile fracture strain in region 3. Terfenol-D has a huge magnetostriction, but extremely poor ductility. The integration of excellent structural and functional properties has been obtained by the combination of trace Tb addition and directional solidification with a ⟨100⟩ single-crystal seed. From the point of view of cost, raw material costs for the Tb-doped FeGa alloys are about eight times lower for Terfenol-D, and they also have less waste in the crystal preparation process.

The influence of Tb on two different scales—a nanometer scale for the modified-$D0_3$ nanoinclusions and a submicron scale for the Tb-rich precipitates—is the origin of the simultaneous improvement of both magnetostriction and ductility.

IV. CONCLUSIONS

There was good agreement between the experimental results for $(Fe_{83}Ga_{17})_{99.9}Tb_{0.1}$ alloys and the growth predicted by PROCAST simulation. The optimal growth rate for high-performance Tb-doped $Fe_{100-x}Ga_x$ ($x = 17, 19$) alloys was established to be 3000 mm/h. $Fe_{83}Ga_{17}$ and $Fe_{81}Ga_{19}$ rods with different Tb concentrations are best prepared with a ⟨100⟩ single-crystal seed at the bottom. The effect of Tb doping on the magnetostriction and tensile fracture strain in the rods is explained by its presence in inclusions on two different scales. The increase in magnetostriction is attributed to the higher density of the nanometer-sized modified-$D0_3$ inclusions induced by traces of Tb. The enhancement in ductility is explained by the concentration of dislocations around the submicron-sized Tb-rich precipitates with the Th_2Zn_{17} structure which can effectively hinder their motion, resulting in higher dislocation density in Tb-doped alloys. The magnetostriction of 387 ppm combined with a remarkable tensile fracture strain of almost 12.5% are obtained in 0.05 at.% Tb-doped $Fe_{81}Ga_{19}$, and represent a significant improvement of ∼29% in magnetostriction and a sixfold enhancement in tensile fracture strain compared with an undoped binary $Fe_{81}Ga_{19}$ single crystal. The integration of useful structural and functional properties that has been obtained by the combination of an appropriate trace rare-earth addition and directional solidification with a ⟨100⟩ single-crystal seed at the bottom is likely to promote more extensive applications of magnetostrictive materials that contain only traces of Tb or another rare earths.

ACKNOWLEDGMENTS

This work was supported by the National Natural Science Foundations of China (NSFC) under Grants No. 51331001, No. 51671011, and No. 51674011, and the China Postdoctoral Science Foundation Funded Project under Grants No. 2017M610738 and No. 2018T110026.

[1] A. E. Clark and M. Wunfogle, Modern magnetostrictive materials: Classical and nonclassical alloys, Proc. SPIE **4699**, 421 (2002).

[2] J. M. D. Coey, *Magnetism and Magnetic Materials* (Cambridge University Press, Cambridge, 2010).

[3] Z. X. Deng and M. J. Dapino, Review of magnetostrictive vibration energy harvesters, Smart Mater. Struct. **26**, 103001 (2017).

[4] J. Atulasimha and A. B. Flatau, A review of magnetostrictive iron-gallium alloys, Smart Mater. Struct. **20**, 043001 (2011).

[5] V. Polewczyk, K. Dumesnil, D. Lacour, M. Moutaouekkil, H. Mjahed, N. Tiercelin, S. Petit Watelot, H. Mishra, Y. Dusch, S. Hage-Ali, O. Elmazria, F. Montaigne, A. Talbi, O. Bou Matar, and M. Hehn, Unipolar and Bipolar High-Magnetic-Field Sensors Based on Surface Acoustic Wave Resonators, Phys. Rev. Appl. **8**, 024001 (2017).

[6] A. Aubert, V. Loyau, Y. Pascal, F. Mazaleyrat, and M. LoBue, Dynamic Magnetostriction of $CoFe_2O_4$ and Its Role in Magnetoelectric Composites, Phys. Rev. Appl. **9**, 044035 (2018).

[7] Y. J. Han, H. Wang, T. L. Zhang, Y. K. He, J. M. D. Coey, and C. B. Jiang, Tailoring the heterogeneous magnetostriction in Fe-Co alloys, J. Alloy. Compd. **699**, 200 (2017).

[8] R. Abbundi and A. E. Clark, Analogus thermal expansion and magnetostriction of single crystal $Tb_{.27}Dy_{.73}Fe_2$, IEEE Trans. Magn. **13**, 1519 (1977).

[9] A. Ktena, C. Manasis, and E. Hristoforou, On the measurement of permeability and magnetostriction in ribbons and wires, IEEE Trans. Magn. **50**, 6100504 (2014).

[10] A. Yamaguchi, K. Motoi, A. Hirohata, H. Miyajima, Y. Miyashita, and Y. Sanada, Broadband ferromagnetic resonance of $Ni_{81}Fe_{19}$ wires using a rectifying effect, Phys. Rev. B **78**, 104401 (2008).

[11] J. B. Restorff, M. Wun-Fogle, K. B. Hathaway, A. E. Clark, T. A. Lograsso, and G. Petculescu, Tetragonal magnetostriction and magnetoelastic coupling in Fe-Al, Fe-Ga, Fe-Ge, Fe-Si, Fe-Ga-Al, and Fe-Ga-Ge alloys, J. Appl. Phys. **111**, 023905 (2012).

[12] C. Bormio-Nunes, C. Paduani, C. T. dos Santos, H. J. Izário Fo, A. A. Coelho, and L. Ghivelder, Magnetostriction of $Fe_{100-x}V_x$ alloys for $5.2 \leqslant x \leqslant 40.7$, J. Alloy. Compd. **553**, 233 (2013).

[13] P. Tayalia, D. Heider, and J. W. Gillespie Jr, Characterization and theoretical modeling of magnetostrictive strain sensors, Sensor. Actuat. A-Phys. **111**, 267 (2004).

[14] A. E. Clark, B. F. DeSavage, and R. Bozorth, Anomalous thermal expansion and magnetostriction of single-crystal dysprosium, Phys. Rev. **138**, A216 (1965).

[15] H. Meng, T. L. Zhang, C. B. Jiang, and H. B. Xu, Grain-⟨111⟩-oriented anisotropy in the bonded giant magnetostrictive material, Appl. Phys. Lett. **96**, 102501 (2010).

[16] T. L. Zhang, C. B. Jiang, X. L. Liu, and H. B. Xu, Dynamic magnetostrain properties of giant magnetostrictive alloy actuators for damping, Smart Mater. Struc. **14**, N38 (2005).

[17] W. Y. Kim and S. Hanada, Tensile elongation of off-stoichiometric Fe_3Si single crystals at high temperatures, J. Alloy. Compd. **299**, 208 (2000).

[18] X. M. Xiao, X. X. Gao, J. H. L, and J. X. Xie, Influence of yttrium on the structure and magnetostriction of $Fe_{83}Ga_{17}$ alloy, Int. J. Min. Met. Mater. **19**, 849 (2012).

[19] A. J. Albaaji, E. G. Castle, M. J. Reece, J. P. Hall, and S. L. Evans, Enhancement in the elongation, yield strength and magnetic properties of intermetallic FeCo alloy using spark plasma sintering, J. Mater. Sci. **52**, 13284 (2017).

[20] R. Kant, U. Prakash, V. Agarwala, and V. V. Satya Prasad, Effect of carbon and titanium additions on mechanical properties of B2 FeAl, T Indian I Metals **69**, 845 (2016).

[21] J. H. Li, X. X. Gao, J. Zhu, X. Q. Bao, T. Xia, and M. C. Zhang, Ductility, texture and large magnetostriction of Fe–Ga-based sheets, Scripta Mater. **63**, 246 (2010).

[22] R. A. Kellogg, A. M. Russell, T. A. Lograsso, A. B. Flatau, A. E. Clark, and M. Wun-Fogle, Mechanical properties of magnetostrictive iron-gallium alloys, Proc. SPIE **5053**, 534 (2003).

[23] T. Atulasimha and A. B. Flatau, Experimental actuation and sensing behavior of single-crystal iron-gallium alloys, J. Intel. Mater. Syst. Struc. **19**, 1371 (2008).

[24] C. Yuan, J. H. Li, W. L. Zhang, X. Q. Bao, and X. X. Gao, Microstructure and magnetostrictive performance of NbC-doped ⟨001⟩ oriented Fe−Ga alloys, Int. J. Min. Met. Mater. **22**, 52 (2015).

[25] Y. Y. Liu, J. H. Li, and X. X. Gao, Effect of Al substitution for Ga on the mechanical properties of directional solidified Fe-Ga alloys, J. Magn. Magn. Mater. **423**, 245 (2017).

[26] B. W. Wang, S. C. Busbridge, Y. X. Li, G. H. Wu, and A. R. Piercy, Magnetostriction and magnetization process of $Tb_{0.27}Dy_{0.73}Fe_2$ single crystal, J. Magn. Magn. Mater. **218**, 198 (2000).

[27] Q. Xing, Y. Du, R. J. McQueeney, and T. A. Lograsso, Structural investigations of Fe-Ga alloys: Phase relations and magnetostrictive behavior, Acta Mater. **56**, 4536 (2008).

[28] J. H. Li, X. X. Gao, J. Zhu, J. Li, and M. C. Zhang, Ductility enhancement and magnetostriction of polycrystalline Fe–Ga based alloys, J. Alloy. Compd. **484**, 203 (2009).

[29] C. Z. Meng, H. Wang, Y. Y. Wu, J. H. Liu, and C. B. Jiang, Investigating enhanced mechanical properties in dual-phase Fe-Ga-Tb alloys, Sci. Rep. **6**, 34258 (2016).

[30] R. A. Kellogg, A. B. Flatau, A. E. Clark, M. Wun-Fogle, and T. A. Lograsso, Temperature and stress dependencies of the magnetic and magnetostrictive properties of $Fe_{0.81}Ga_{0.19}$, J. Appl. Phys. **91**, 7821 (2002).

[31] C. Bormio-Nunes, C. T. dos Santos, I. F. Leandro, R. S. Turtelli, R. Grössinger, and M. Atif, Improved magnetostriction of $Fe_{72}Ga_{28}$ boron doped alloys, J. Appl. Phys. **109**, 07A934 (2011).

[32] H. Basumatary, M. Palit, J. A. Chelvane, S. Pandian, M. M. Raja, and V. Chandrasekaran, Beneficial effect of boron on the structural and magnetostrictive behavior of $Fe_{77}Ga_{23}$ alloy, J. Magn. Magn. Mater. **322**, 2769 (2010).

[33] S. Guruswamy, N. Srisukhumbowornchai, A. E. Clark, J. B. Restorff, and M. Wun-Fogle, Strong, ductile and low-field-magnetostrictive alloys based on Fe-Ga, Scr. Mater. **43**, 239 (2000).

[34] S. M. Na and A. B. Flatau, Deformation behavior and magnetostriction of polycrystalline Fe-Ga-X, (X = B, C, Mn, Mo, Nb, NbC) alloys, J. Appl. Phys. **103**, 07D304 (2008).

[35] T. Takahashi, T. Okazaki, and Y. Furuya, Improvement in the mechanical strength of magnetostrictive (Fe-Ga-Al)-X-C (X = Zr, Nb and Mo) alloys by carbide precipitation, Scr. Mater. **61**, 5 (2009).

[36] A. L. Sun, J. H. Liu, and C. B. Jiang, Dual-reinforcement $(TaC_{particle} + TaC_{dendrite})$/FeGa magnetostrictive composites, Mater. Sci. Eng. A **639**, 370 (2015).

[37] C. Bormio-Nunes, R. S. Turtelli, H. Mueller, R Grössinger, H. Sassik, and M. A. Tirelli, Magnetostriction and structural characterization of Fe-Ga-X (X = Co, Ni, Al) mold-cast bulk, J. Magn. Magn. Mater. **290-291**, 820 (2005).

[38] T. A. Lograsso, N. J. Jones, D. L. Schlagel, G. Petculescu, M. Wun-Fogle, J. B. Restorff, A. E. Clark, and K. B. Hathaway, Effects of Zn additions to highly magnetoelastic FeGa alloys, J. Appl. Phys. **117**, 17E701 (2015).

[39] A. E. Nolting and E. Summers, Tensile properties of binary and alloyed Galfenol, J. Mater. Sci. **50**, 5136 (2015).

[40] L. P. Jiang, J. D. Yang, H. B. Hao, G. R. Zhang, S. X. Wu, Y. J. Chen, O. Obi, T. Fitchorov, and V. G. Harris, Giant enhancement in the magnetostrictive effect of FeGa alloys doped with low levels of terbium, Appl. Phys. Lett. **102**, 222409 (2013).

[41] W. Wu, J. H. Liu, C. B. Jiang, and H. B. Xu, Giant magnetostriction in Tb-doped $Fe_{83}Ga_{17}$ melt-spun ribbons, Appl. Phys. Lett. **103**, 262403 (2013).

[42] Y. K. He, X. Q. Ke, C. B. Jiang, N. H. Miao, H. Wang, J. M. D. Coey, Y. Z. Wang, and H. B. Xu, Interaction of trace rare-earth dopants and nanoheterogeneities induces giant magnetostriction in Fe-Ga alloys, Adv. Funct. Mater. **28**, 1800858 (2018).

[43] Y. K. He, C. B. Jiang, W. Wu, B. Wang, H. P. Duan, H. Wang, T. L. Zhang, J. M. Wang, J. H. Liu, Z. L. Zhang, P. Stamenov, J. M. D. Coey, and H. B. Xu, Giant heterogeneous magnetostriction in Fe-Ga alloys: Effect of trace element doping, Acta Mater. **109**, 177 (2016).

[44] T. Y. Ma, S. S. Hu, G. H. Bai, M. Yan, Y. H. Lu, H. Y. Li, X. L. Peng, and X. B. Ren, Structural origin for the local strong anisotropy in melt-spun Fe-Ga-Tb: Tetragonal nanoparticles, Appl. Phys. Lett. **106**, 112401 (2015).

[45] C. Z. Meng and C. B. Jiang, Magnetostriction of a $Fe_{83}Ga_{17}$ single crystal slightly doped with Tb, Scr. Mater. **114**, 9 (2016).

[46] Z. B. Wang, J. H. Liu, and C. B. Jiang, Magnetostriction of $Fe_{81}Ga_{19}$ oriented crystals, Chin. Phys. B **19**, 117504 (2010).

[47] C. Li, J. H. Liu, Z. B. Wang, and C. B. Jiang, Crystal growth of high magnetostrictive polycrystalline $Fe_{81}Ga_{19}$ alloys, J. Magn. Magn. Mater. **324**, 1177 (2012).

[48] A. J. Elliott, Directional solidification of large cross-section Ni-base superalloy casting via liquid metal cooling, Ph.D. thesis (The University of Michigan University, 1980).

[49] D. Z. Kang, J. H. Liu, C. B. Jiang, and H. B. Xu, Control of solid-liquid interface morphology and radial composition distribution: TbDyFe single crystal growth, J. Alloy. Compd. **621**, 331 (2015).

[50] C. B. Jiang, J. H. Liu, J. M. Wang, L. H. Xu, and H. B. Xu, Solid-liquid interface morphology and crystal growth of NiMnGa magnetic shape memory alloys, Acta Mater. **53**, 1111 (2005).

[51] L. Y. Yang, S. M. Li, X. Q. Chang, H. Zhong, and H. Z. Fu, Twinned dendrite growth during Bridgman solidification, Acta Mater. **97**, 269 (2015).

[52] C. Z. Meng, Y. Y. Wu, and C. B. Jiang, Design of high ductility FeGa magnetostrictive alloys: Tb doping and directional solidification, Mater. Des. **130**, 183 (2017).

[53] Y. J. Han, Hui Wang, T. L. Zhang, Y. K. He, and C. B. Jiang, Exploring structural origin of the enhanced magnetostriction in Tb-doped $Fe_{83}Ga_{17}$ ribbons: Tuning Tb solubility, Scr. Mater. **150**, 101 (2018).

[54] W. Wu, J. H. Liu, and C. B. Jiang, Tb solid solution and enhanced magnetostriction in $Fe_{83}Ga_{17}$ alloys, J. Alloy. Compd. **622**, 379 (2015).

[55] V. V. Palacheva, A. Emdadi, F. Emeis, I. A. Bobrikov, A. M. Balaguro, S. V. Divinski, G. Wilde, and I. S. Golovin, Phase transitions as a tool for tailoring magnetostriction in intrinsic Fe-Ga composites, Acta Mater. **130**, 229 (2017).

[56] I. S. Golovin, A. M. Balagurov, V. V. Palacheva, A. Emdadi, I. A. Bobrikov, A. Yu. Churyumov, V. V. Cheverikin, A. V. Pozdniakov, A. V. Mikhaylovskaya, and S. A. Golovin, Influence of Tb on structure and properties of Fe-19%Ga and Fe-27%Ga alloys, J. Alloy. Compd. **707**, 51 (2017).

[57] J. B. Restorff, M. Wun-Fogle, and A. E. Clark, Temperature and stress dependences of the magnetostriction in ternary and quaternary Terfenol alloys, J. Appl. Phys. **87**, 5786 (2000).

[58] A. E. Clark, M. Wun-Fogle, J. B. Restorff, and T. A. Lograsso, Magnetostrictive properties of galfenol alloys under compressive stress, Mater. Trans. **43**, 881 (2002).

[59] A. E. Clark, K. B. Hathaway, M. Wun-Fogle, J. B. Restorff, T. A. Lograsso, V. M. Keppens, G. Petculescu, and R. A. Taylor, Extraordinary magnetoelasticity and lattice softening in bcc Fe-Ga alloys, J. Appl. Phys. **93**, 8621 (2003).

[60] A. E. Clark, J. B. Restorff, M. Wun-Fogle, T. A. Lograsso, and D. L. Schlagel, Magnetostrictive properties of body-centered cubic Fe-Ga and Fe-Ga-Al alloys, IEEE Trans. Magn. **36**, 3238 (2000).

[61] Y. Wu, L. Fang, C. Meng, Y. Chen, J. Wang, J. Liu, T. Zhang, and C. Jiang, Improved magnetostriction and mechanical properties in dual-phase FeGa single crystal, Mater. Res. Lett. **6**, 327 (2018).

[62] O. Ikeda, R. Kainuma, I. Ohnuma, K. Fukamichi, and K. Ishida, Phase equilibria and stability of ordered b.c.c. phases in the Fe-rich portion of the Fe-Ga system, J. Alloy. Compd. **347**, 198 (2002).

[63] T. A. Lograsso, A. R. Ross, D. L. Schlagel, A. E. Clark, and M. Wun-Fogle, Structural transformations in quenched Fe–Ga alloys, J. Alloy. Compd. **350**, 95 (2003).

[64] H. Cao, P. M. Gehring, C. P. Devreugd, J. A. Rodriguez-Rivera, J. Li, and D. Viehland, Role of Nanoscale Precipitates on the Enhanced Magnetostriction of Heat-Treated Galfenol ($Fe_{1-x}Ga_x$) Alloys, Phys. Rev. Lett. **102**, 127201 (2009).

[65] M. Laver, C. Mudivarthi, J. R. Cullen, A. B. Flatau, W.-C. Chen, S. M. Watson, and M. Wuttig, Magnetostriction and Magnetic Heterogeneities in Iron-Gallium, Phys. Rev. Lett. **105**, 027202 (2010).

[66] W. F. Rao, M. Wuttig, and A. G. Khachaturyan, Giant Nonhysteretic Responses of Two-Phase Nanostructured Alloys, Phys. Rev. Lett. **106**, 105703 (2011).

[67] A. Kumagai, A. Fujita, K. Fukamichi, K. Oikawa, R. Kainuma, and K. Ishida, Magnetocrystalline anisotropy and magnetostriction in ordered and disordered Fe-Ga single crystals, J. Magn. Magn. Mater. **272–276**, 2060 (2004).

[68] H. Zhang, T. L. Zhang, and C. B. Jiang, Magnetostrictive actuators with large displacement and fast response, Smart Mater. Struc. **21**, 055014 (2012).

[69] H. Zhang, T. L. Zhang, and C. B. Jiang, Design of a uniform bias magnetic field for giant magnetostrictive actuators applying triple-ring magnets, Smart Mater. Struc. **22**, 115009 (2013).

[70] A. García-Arribas, J. Gutiérrez, G. V. Kurlyandskaya, J. M. Barandiarán, A. Svalov, E. Fernández, A. Lasheras, D. de Cos and I. Bravo-Imaz, Sensor applications of soft magnetic materials based on magneto-impedance, magneto-elastic resonance and magneto-electricity, Sensors **14**, 7602 (2014).